Received: 24 May 2018 | Revised: 17 August 2018 | Accepted: 21 October 2018 | Published on: 26 November 2018

DOI: 10.1002/joc.5909

International Journal of Climatology RMetS

RESEARCH ARTICLE

The interannual variability of wind energy resources across China and its relationship to large-scale circulation changes

Lejiang Yu[1,2] | Shiyuan Zhong[2] | Xindi Bian[3] | Warren E. Heilman[3]

[1]SOA Key Laboratory for Polar Science, Polar Research Institute of China, Shanghai, China

[2]Department of Geography, Environment and Spatial Sciences, Michigan State University, East Lansing, Michigan

[3]Northern Research Station, US Forest Service, Lansing, Michigan

Correspondence
Shiyuan Zhong, Department of Geography, Environment and Spatial Sciences, Michigan State University, 674 Auditorium Rd., East Lansing, MI 48824.
Email: zhongs@msu.edu

Funding information
Shanghai Pujiang Program, Grant/Award Number: No. 17PJ1409800

This study investigates the interannual variability of wind energy resources across China and how it changes with season by applying empirical orthogonal function (EOF) analyses to gridded wind data from the Climate Forecast System Reanalysis (CFSR) from January 1979 through December 2011. The first EOF mode (EOF1) represents between 22% variance for winter and 29% for summer. Spatially, the variation is largely consistent across China for summer and autumn and almost opposite between north and south for spring and winter, and the strongest variation in all seasons is found over Inner Mongolia and Tibet. The second EOF mode (EOF2) represents between 13% variance for autumn and 16% for spring, and is largely dominated by a sharp contrast between Inner Mongolia and Tibet for all seasons. The EOF1 appears to be linked statistically to the pacific decadal oscillation for summer and autumn and to the Pacific North American pattern for spring and winter, while the EOF2 seems to be connected to the Arctic Oscillation for spring and winter and to an interdecadal variability for summer and autumn. The anomalous wind fields associated with these large-scale circulation patterns modify the climatological wind fields in different ways that lead to an increase or a decrease of the 80-m winds in different regions of China.

KEYWORDS
climate forecast system reanalysis, climate variability, seasonal prediction, statistical analysis

1 | INTRODUCTION

Since China's Renewable Energy Law took effect in January 2006, the country has seen a rapid growth in its renewable energy sector. Leading the way is wind energy, with the cumulative installed capacity increasing exponentially from less than 2 gigawatts (GW) in 2005 to 45 GW in 2010 (Jiang *et al.,* 2011), and it is projected to reach between 200 and 300 GW by 2020 and over 400 GW by 2030 (Li *et al.,* 2012). Wind energy has been the fastest growing source of electricity in China and a key stimulating factor of Chinese economic growth.

For wind resource assessment and wind power forecasting, it is important to know not only the mean wind speed, but also the variability. While a number of previous studies have examined trends and seasonal variability of wind resources in different regions of China (Zuo *et al.,* 2005; Xu *et al.,* 2006; Niu *et al.,* 2010; Fu *et al.,* 2011; Jiang *et al.,* 2013; Lin *et al.,* 2013; Yao and Li, 2016; Yu *et al.,* 2016), few studies have investigated interannual variability of wind resources across entire China.

A key influential factor for interannual variability of low-level winds in China, especially Eastern China, is the East Asian monsoon (Wang and Lin, 2002). Numerous studies have linked the interannual variability of the East Asian monsoon to well-known climate variability modes such as

the Arctic oscillation (Gong *et al.,* 2001; Gong and Ho, 2003), the El Niño Southern Oscillation (ENSO) (Wang *et al.,* 2000), the Pacific Decadal Oscillation (PDO) (Chan and Zhou, 2005; Yoon and Yeh, 2010) and the North Atlantic Oscillation (NAO) (Watanabe, 2004; Wu *et al.,* 2009). While the identification of these teleconnections has led to improved seasonal predictions of the East Asian monsoon and thus wind power in monsoon-influenced region of Eastern China, it has limited value for seasonal outlook and long-term predictions of wind power output in other parts of the country such as Inner Mongolia, the Northwest, and the Tibetan Plateau where the best wind resources are located (McElroy *et al.,* 2009).

The purpose of this study is to further our understanding of wind power variability at interannual time scales across China and the potential connections between the interannual variability and known climate variability modes. Several studies have examined this issue. For example, Fu *et al*. (2011) examined the variability of 10-m wind speeds at 597 observational stations across China and linked the variability to the Interdecadal Pacific Oscillation. Chen *et al*. (2013) found a significant negative correlation between spatially averaged annual 10-m wind speeds across China and the annual AO indices. They also found that during El Niño episodes, the annual mean wind speeds tend to be above normal in northern China and below normal in southern China, with the opposite occurring during La Niña episodes. Zhang *et al*. (2014) showed that the Tibetan monsoon contributes to the changes of wind speeds in southwestern China. Cui *et al*. (2018) noted that the temporal variation of the near-surface winds in northern China is related to changes in the East Asian monsoon and westerly circulation. Besides natural factors, anthropogenic factors such as changes in roughness lengths resulting from urbanization and deforestation also have a strong influence on surface wind speeds over East China (Wu *et al.,* 2016, 2017; Zha *et al.,* 2017). The value of these studies for understanding wind energy variability in China, however, is limited by the use of 10-m standard wind observations because (a) many of the meteorological observational stations in China are located in sheltered settings, while wind turbine sites are often located on ridges or open terrain; (b) changes in the locations and environment around observational sites, which are exacerbated by the rapid urbanization across China in the past three decades, may lead to discontinuities in the observational data; (c) 10-m wind speeds are more prone to the influence of the underlying terrain than winds at modern wind turbine levels; and (d) the heterogeneous distribution of observational stations hinders the understanding of the spatial variability of wind energy resources.

The current analyses try to overcome these issues by using gridded wind data at the modern wind turbine level (80 m above ground level (AGL)). This study identifies and characterizes the main modes of the 80-m wind interannual variability across China and the dominant climate forcing for these modes. Understanding the low-frequency variability of wind speeds, or how and why wind speed and wind power vary from 1 year to another, can be beneficial for seasonal outlooks or long-range forecasting of wind power generation (Westrick *et al.,* 2005).

2 | DATASETS AND METHODS

2.1 | Study domain and datasets

The domain of the current study encompasses a region from 18°N to 54°N and from 73°E to 136°E (Figure 1), but the discussion will focus only on the land areas of China. The analyses span a 33-year period from January 1, 1979 to December 31, 2011.

Wind speed data for the study period and the domain are extracted from the gridded CFSR produced by the U.S. National Centers for Environmental Prediction (NCEP) using a global, high-resolution, coupled modelling system with atmosphere, ocean, land-surface and sea-ice models (Saha *et al.,* 2010). The gridded wind data have a horizontal resolution of ~38 km (T382) on 64 vertical levels from the surface to 0.26 hPa in the atmosphere. As a third-generation global reanalysis, the CFSR has several advanced features compared to earlier generation reanalysis products, which includes a 6-hour guess field generated from an atmosphere and ocean coupling system, an interactive sea-ice model, direct assimilation of satellite radiances and consideration of changes of carbon dioxide (CO_2), aerosols and other trace gases and solar activity. For details about the CFSR, refer to Saha *et al*. (2010). The latest version (Version 2) of CFSR (CFSv2) (Saha *et al.,* 2014) is used in this analysis.

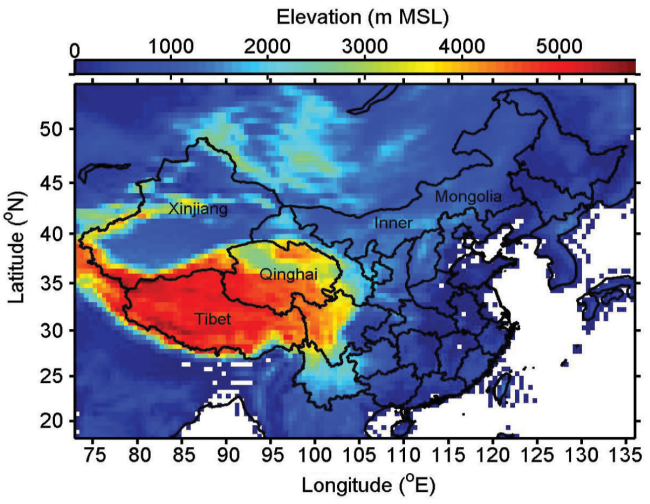

FIGURE 1 The study domain (18°N-54°N, 74°E-135°E) and the topography as resolved by the CFSR data [Colour figure can be viewed at wileyonlinelibrary.com]

CFSR wind data in regions of China have been compared to observations and other reanalysis products. Bao and Zhang (2013) found that horizontal wind components from the CFSR agree with data from soundings launched during the Tibetan Plateau Experiment and have smaller root-mean-square values compared to those of the NCEP reanalyses and Interim European Centre for Medium-Range Weather Forecasts Re-Analysis (ERA-Interim, Dee *et al.,* 2011). Rahim *et al*. (2013) showed that wind speed time series from the CFSR are similar to the time series derived from satellite observations over the South China Sea, with a correlation coefficient of 0.94 for the period of September 2008 to January 2009. However, the magnitudes of wind speed from the CFSR are somewhat lower than the values derived from satellite observations. Chen *et al*. (2014) evaluated the diurnal cycle of wind data from four reanalysis products, including CFSR, ERA-Interim, the 55-year Japanese reanalysis project (JRA-55, Ebita *et al.,* 2011), and National Aeronautics and Space Administration Modern-Era Retrospective Analysis for Research and Applications (MERRA, Rienecker *et al.,* 2011), using 6-hour rawinsonde observations from 22 sites over southern China, and they found that the four reanalysis datasets adequately capture the observed mean diurnal cycle, but the amplitudes of the diurnal cycles differ among the four datasets and from the observations.

In addition to the CFSR, the analyses here also utilize the U.S. National Oceanic and Atmospheric Administration Extended Reconstructed Sea Surface Temperature (SST) data (http://www.esrl.noaa.goc/psd/data/gridded/data.noaa.ersst.html), as well as time series of several climate indices including the PDO index (Mantua *et al.,* 1997) (http://research.jisao.washington.edu/pdo/) and the AO index (http://www.cpc.ncep.noaa.gov/data/indices).

2.2 | Methods

The vertical resolution of the CFSRv2 wind data is 25 hPa from 1,000 to 750 hPa and 50 hPa above that. In addition, wind speeds at the 10-m level are also available. There are several ways to estimate wind speed at a given level (80 m in this case). When only surface winds are available, the power law (Hsu *et al.,* 1994) is usually used to extrapolate surface wind to a chosen level aloft within the atmospheric boundary layer. Sometime a log profile (Stull, 1988) is also used to extrapolate surface wind to a level in the surface layer which is about 10% of the boundary layer height. When vertical wind profiles are available, a simple linear interpolation or the log profile is usually used to obtain wind speed at a given level. The log profile is considered more accurate for estimating winds in the surface layer. Although surface layers can be deeper than 80 m in unstable conditions, they are usually lower than 80 m in neutral and stable conditions. Note that the coefficients in the log profile equation (friction velocity and roughness length) can be determined by wind profiles only in the case of neutral conditions; in non-neutral conditions, temperature profiles are also needed to define the stability term in the log profile. Based on these considerations, simple linear interpolation is utilized in this study to estimate the 80-m level wind from the 10 m wind speed and the wind speed at the first level immediately above the 80 m level, although linear interpolation tends to underestimate 80-m winds compared to the log profile.

The temporal resolutions of the CFSRv2 wind data are 6-hourly, which are averaged to yield daily, monthly and seasonal means for spring (March, April, May), summer (June, July, August), autumn (September, October, November) and winter (December, January, February). Finally, seasonal anomalies are computed by subtracting seasonal climatology relative to the study period (averaging over the 33 years) from the seasonal means for each year.

The EOF technique is applied to the gridded seasonal anomalies of 80-m wind speeds to identify possible spatial patterns of the variability and how they change with time. Using this technique, the anomalous wind fields are partitioned into a set of mathematically orthogonal modes consisting of spatial structures (EOFs) and corresponding time series referred to as principal components (PCs), and each mode has a corresponding eigenvalue that describes the variance explained by the mode (Wilks, 2011). The current analyses focus on the first two EOF modes (EOF1 and EOF2) that together explain a large percentage of the total variance. Linear regression (Neter *et al.,* 1996; Draper and Smith, 1998) is performed in which the seasonal anomalies of SST and atmospheric fields for the same study period are regressed onto the PC of the first two EOF modes to determine the anomalous large-scale circulation patterns associated with the EOF modes.

3 | RESULTS

3.1 | The first EOF mode

The first EOF mode (EOF1, Figure 2) explains 20–30% of the total variance in seasonal 80-m wind speed anomalies, with percentages ranging from 21.5% for the winter season to 29.4% for the summer season. The EOF1 spatial patterns are similar between spring and winter, and between summer and autumn. For spring (Figure 2a) and winter (Figure 2g), the variations are opposite in sign between northern and southern China separated roughly by the 36°N latitude line, with strongest contrast between Inner Mongolia (negative) and Tibet (positive). The time series for the two seasons, however, are poorly correlated, with the spring time series (Figure 2b) oscillates around zero prior to 2005 and drops to all negative values afterwards, while winter time series (Figure 2e) keeps oscillating

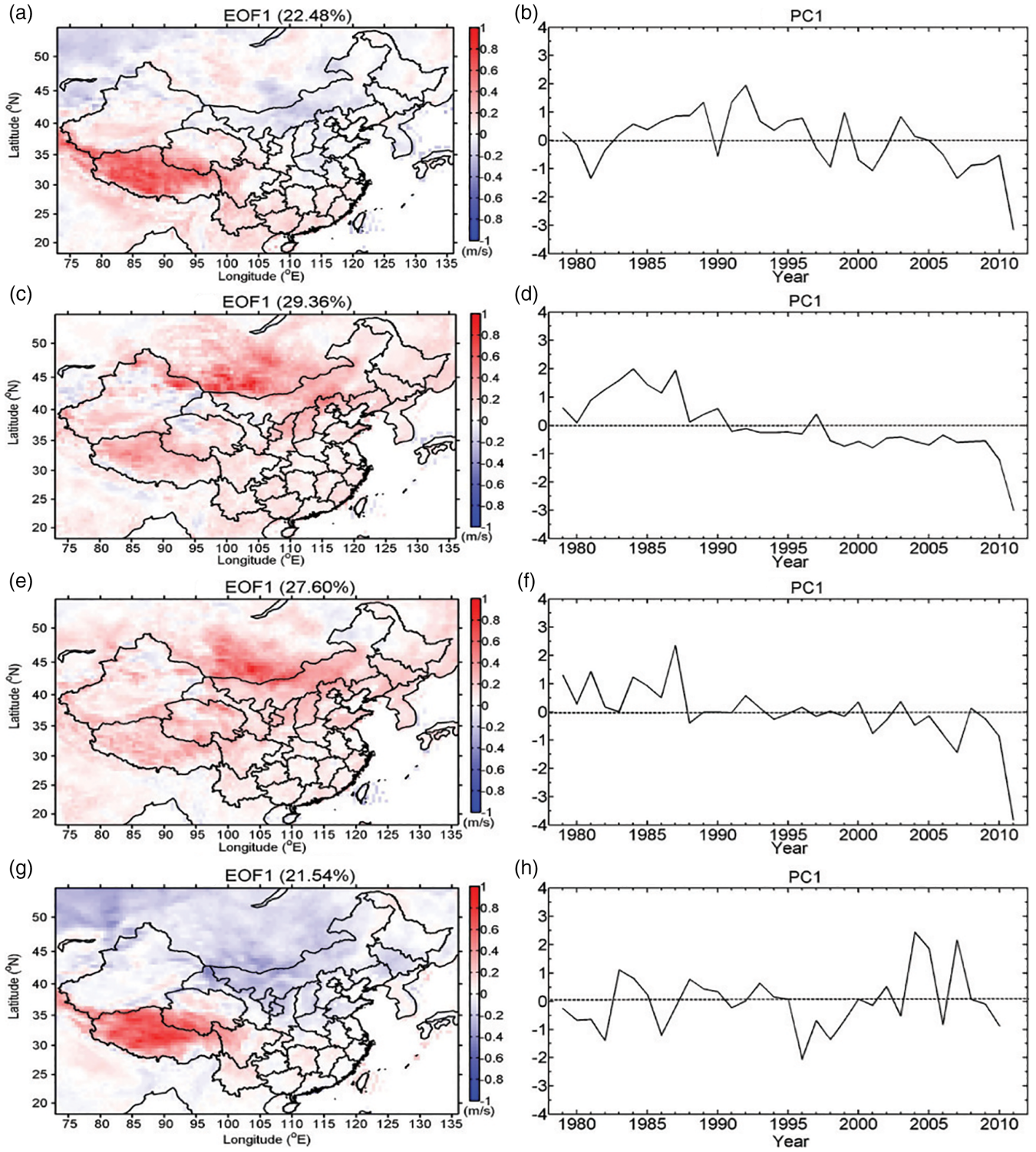

FIGURE 2 EOF1 spatial patterns (a, c, e, g) and time series (b, d, f, h) for the 80-m wind speed seasonal anomalies for spring (a, b), summer (c, d), autumn (e, f) and winter (g, h) for the period 1979 to 2011 [Colour figure can be viewed at wileyonlinelibrary.com]

throughout the study period. Different from spring and winter, the EOF1 spatial patterns for summer and autumn show more or less consistent variations across most of China except for small areas in the northwest, where variations are in opposite direction to the rest of the country. With a correlation coefficient of 0.80 at the 99.9% confidence level, the summer and autumn time series show a very similar pattern with values all positive in the 1980s, oscillating around zero in the 1990s, and all negative after 2000. Both time series are characterized by a decreasing trend with a slope of −0.08/yr and −0.07/yr, respectively, at the 98% confidence level. The PC1s for summer and autumn are correlated with the PDO indices, which show decreasing trends for the period of 1979 through 2011 at the rates of −0.05/yr for summer and − 0.06/yr for autumn at the 98% confidence level (Figure 3). The correlation coefficients are

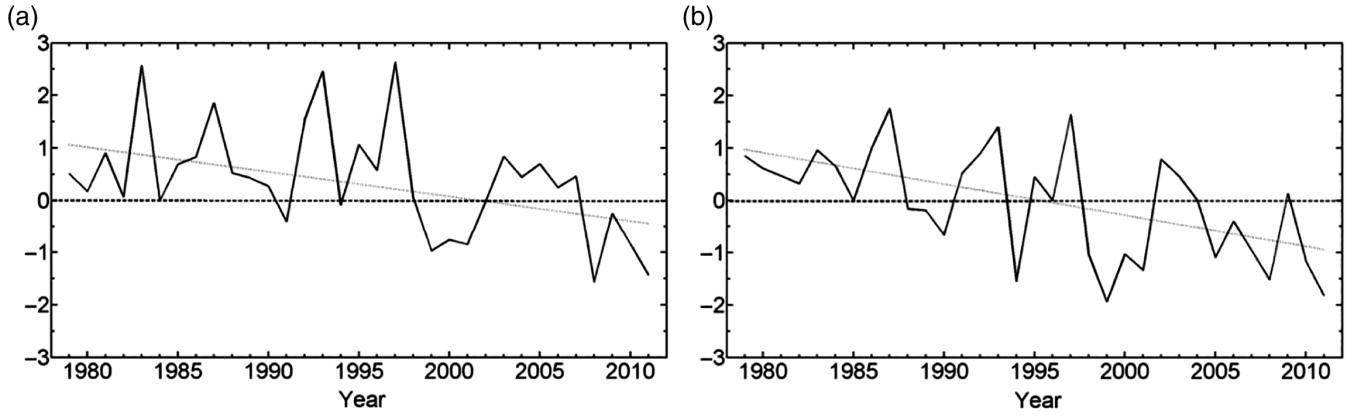

FIGURE 3 The time series of the PDO index for summer (a) and autumn (b) for the period 1979 to 2011. Grey dotted line indicates the linear trend

0.54 between the summer PC1 and PDO, and 0.58 between the autumn PC1 and PDO.

To understand the EOF1 spatial patterns and their seasonal differences in the context of atmospheric circulation anomalies, the PC1s are regressed onto the anomalous SST, 200-hPa geopotential height (H200), sea-level pressure, and 80-m wind fields. The results of the regression analyses are shown in Figures 4–7.

The spring SST regression pattern shows positive SST anomalies off the coast of North America and eastern tropical Pacific Ocean and negative SST anomalies in western Pacific Ocean, which resembles positive phase of PDO and ENSO. The SST pattern over the Pacific Ocean excites a wavetrain with positive H200 anomalies over Canada and negative H200 anomalies over the United States and the eastern Pacific Ocean (Figure 5). The Rossby wave extends to the Eurasia continent with positive H200 anomalies over the northern Europe and negative H200 anomalies over the rest of Eurasia and northern Africa. Negative H200 anomalies also occur over China, especially over the northwestern portions of the country. Negative sea-level pressure anomalies as large as −135 Pa also occur over China except for the northeastern part of the country (Figure 6a). The anomalous surface low over northwestern China induces westerly anomalous winds over the Tibetan Plateau (Figure 7a), which reinforces the climatological 80-m wind field (Figure 8a) to produce positive wind speed anomalies in the region (Figure 2a). Similarly, the anomalous easterly winds over southern Xinjiang are in the same direction as the climatological wind fields (Figures 7a and 8a) and thus contribute to the positive 80-m wind anomalies there (Figure 2a). In contrary, anomalous northerly winds around the anomalous surface high north of Xinjiang oppose the climatological southerly winds and lead to negative 80-m wind speed anomalies in that region (Figure 2a). Anomalous southeasterly winds over northern China associated with the negative pressure anomaly centre over western China and the positive pressure anomaly centre over northeastern China oppose the climatological wind and lead to the negative wind speed anomalies over northern China (Figure 2a). The positive wind speed anomalies over southern China also result from the consistency between the anomalous and the climatological wind fields.

In contrast to the spring season, SST regression patterns in summer and autumn resemble an El Niño pattern and a positive phase PDO, with negative SST anomalies over central and tropical western Pacific Oceans and positive SST anomalies over the northeastern and tropical central and eastern Pacific Oceans (Figure 4b,c). The H200 regression maps for summer and autumn are similar over the Eurasia continent, the Pacific Ocean and North America, with positive values over central Asia, central Russia and northwestern North America, and negative values over Europe, East Asia and the North Pacific Ocean (Figure 5b,c). Negative height anomalies occur over the study region with the minimum value of −198 Pa over Mongolia (Figure 6b). The negative pressure centre over Mongolia results in westerly anomalous winds in northern China, particularly Inner Mongolia, and over Tibet (Figure 7b) that reinforce climatological winds (Figure 8b) and yield positive 80-m wind speed anomalies in these regions (Figure 2c).

The winter SST regression exhibits a La Niña pattern (Figure 4d) characterized by negative anomalies in the eastern equatorial Pacific. The corresponding anomalous H200 pattern shows a wavetrain with wave number two over the mid-latitude region and wave number three over the subtropical region (Figure 5d). The positive anomalous H200 values across most of China weaken the trough over East Asia. Much of China except for Tibet is dominated by positive sea-level pressure anomalies (Figure 6d). Associated with the pressure anomalies are anomalous northeasterly and easterly winds in regions north of 35°N (Figure 7d) that are opposite to the southwesterly and westerly climatological wind fields (Figure 8d) and explain the negative wind speed anomalies (Figure 2d). Over the Tibetan Plateau and southern China, the anomalous westerly and northeasterly winds

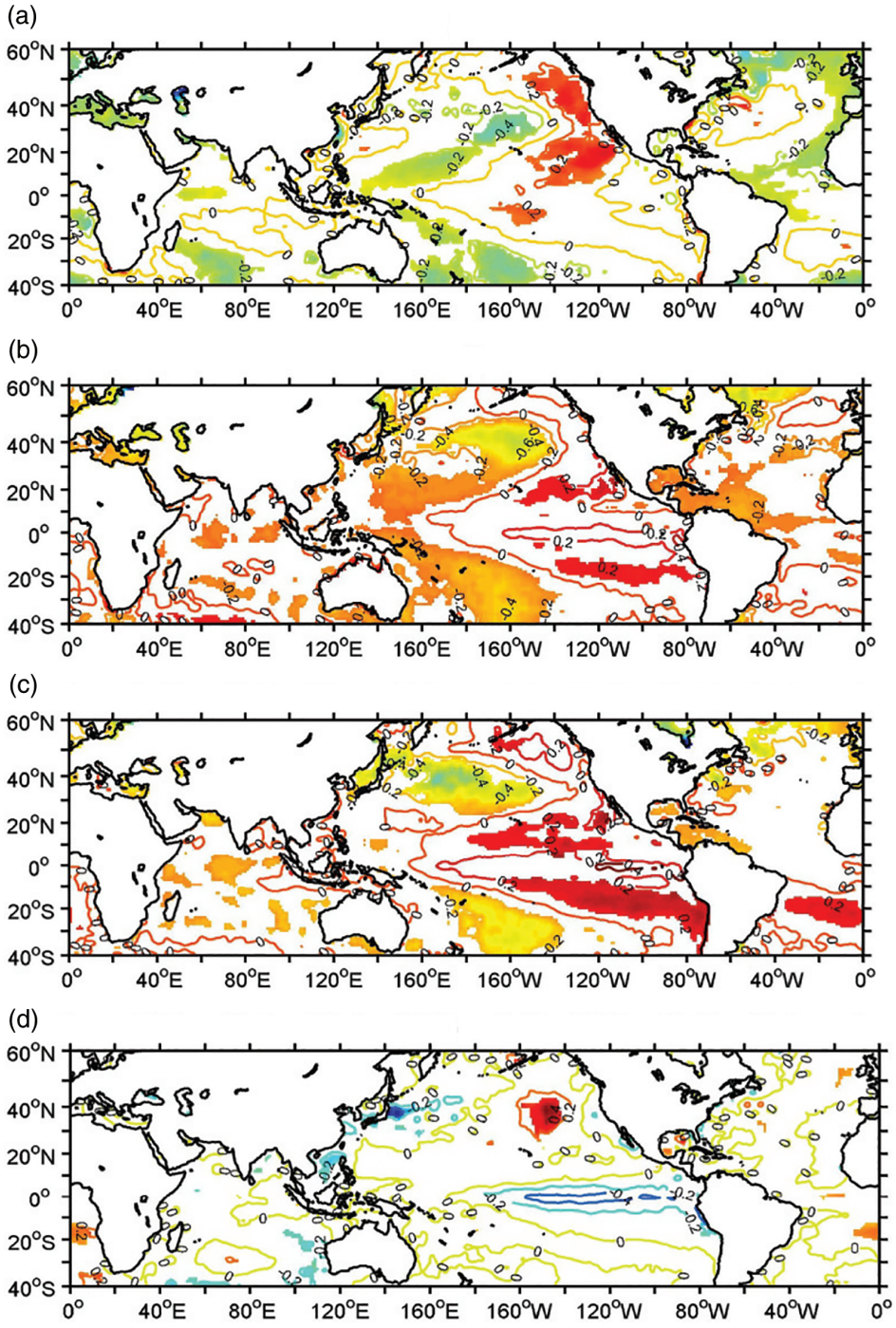

FIGURE 4 The anomalous SST regressed onto the PC1 of the 80-m wind speed seasonal anomalies for spring (a), summer (b), autumn (c), and winter (d) for the period 1979–2011. The colour filled regions are significant at the 95% confidence level [Colour figure can be viewed at wileyonlinelibrary.com]

are in agreement with the climatological wind directions and explain the positive wind speed anomalies in these regions (Figure 2d).

To further confirm the relationship between the 80-m wind speeds and the PDO indices in summer and autumn, correlations between 80-m wind speeds and the PDO indices in summer and autumn are computed at each grid point, and the spatial patterns of the correlations are shown in Figure 9. For both seasons, the correlation field shows a similar spatial pattern to the EOF1 pattern (Figure 2c,e). In the summer, negative correlations occur mainly over the northwestern and northeastern portions of China, while positive correlations occur in most other parts of the country. The most significant correlations occur in regions of the northern and southwestern China and over the Tibetan Plateau. Similarly in autumn, significant positive correlations occur in northern China. Positive correlations are seen across the country with the exception of northern Inner Mongolia and portions of northwestern and

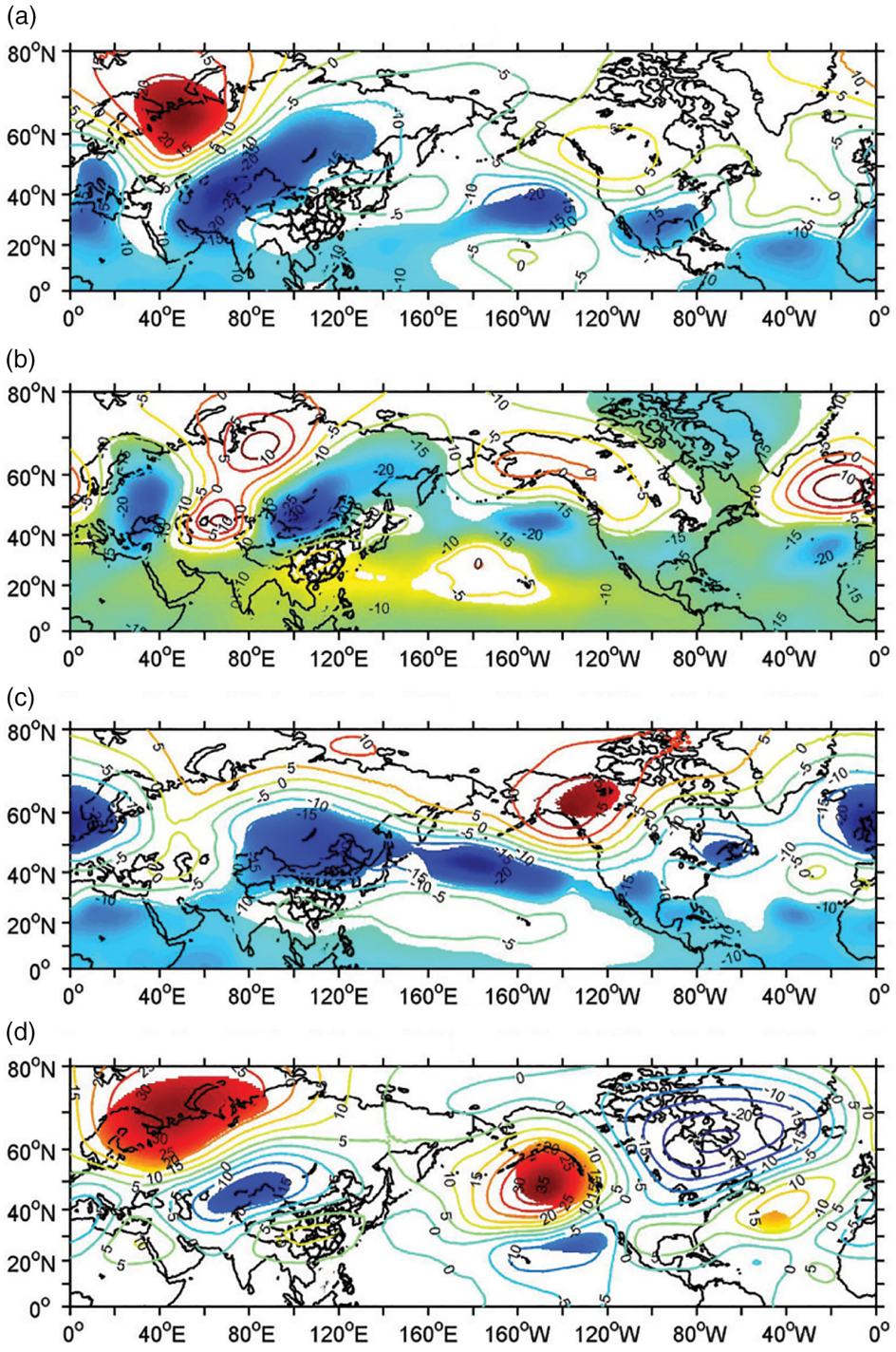

FIGURE 5 The anomalous 200-hPa geopotential heights regressed onto the PC1 of the 80-m wind speed seasonal anomalies for spring (a), summer (b), autumn (c), and winter (d) for the period 1979 to 2011. The colour filled regions are significant at the 95% confidence level [Colour figure can be viewed at wileyonlinelibrary.com]

southern China. These results further indicate that the PDO has a significant influence on 80-m level wind speed variability across China in summer and autumn and is a major contributor to the decreasing trends in these seasons.

3.2 | The second EOF mode

The amounts of the total variances of the seasonal 80-m wind speed anomalies explained by the second EOF modes (EOF2) vary narrowly from 13.3% for autumn to 15.7% for spring. The spatial pattern of the spring season EOF2 is characterized by negative anomalies over the Tibetan Plateau and portions of northwestern China, and positive anomalies throughout the rest of the country, especially in the north and northeast (Figure 10a). The spring PC2 time series is inversely related to the AO index, with a correlation coefficient of −0.40 at the 95% confidence level (Figure 10b). The summer and autumn EOF2 patterns are

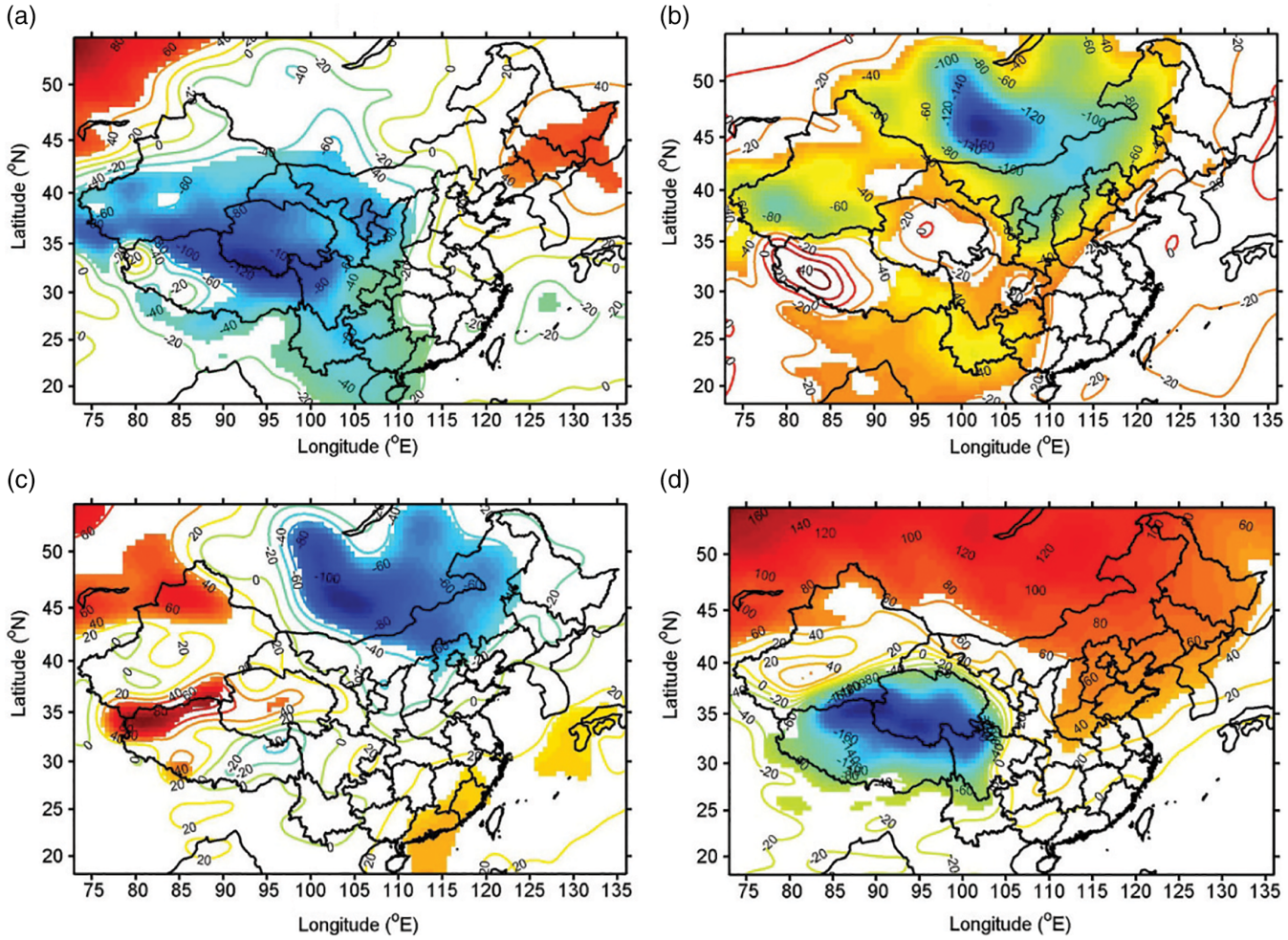

FIGURE 6 The anomalous sea-level pressures regressed onto the PC1 of the 80-m wind speed seasonal anomalies for spring (a), summer (b), autumn (c), and winter (d) for the period 1979 to 2011. The colour filled regions are significant at the 95% confidence level [Colour figure can be viewed at wileyonlinelibrary.com]

characterized by positive anomalies mainly in Inner Mongolia and Xinjiang and negative anomalies in all other regions, particularly over the Tibetan Plateau (Figure 10c and e). The summer and autumn PC2 time series (Figure 2d,f) display variability at interdecadal time scales, where negative values are prevalent over the 1988 to 2008 period and positive values are prevalent before and after that period. The winter EOF2 pattern is characterized by negative wind speed anomalies over southern Tibet and strong positive anomalies over Qinghai and Inner Mongolia (Figure 10g). Weaker positive anomalies also occur over portions of northwestern, north-central, and northeastern China. Similar to spring, a significant correlation (correlation coefficient of −0.62 at the 99.9% confidence level) also exists between the winter season PC2 time series and the AO index.

To explain the EOF2 patterns, linear regression is performed where the anomalous H200, sea-level pressure and 80-m wind fields are regressed to the PC2 for each of the four seasons. The results are shown in Figures 11–13. For the spring season, the H200 regression pattern resembles the negative phase of the AO (Figure 11a), as indicated by significant positive values in the high-latitude regions and West Asia and significant negative values in Europe and Mongolia. The negative H200 anomalies over Mongolia extend southward to northern and central China. The strong surface cyclonic flows (Figure 13a) reinforce the climatological wind pattern and lead to positive wind speed anomalies across most of China except for parts of the northwest and Tibet (Figure 10a). A smaller anomalous high pressure centre exists over Qinghai (Figure 12a), and the corresponding anticyclonic cell (Figure 13a) produces easterly flows that oppose the climatological winds and result in negative wind speed anomalies over Tibet and portions of northwestern China (Figure 10a).

Compared to spring, the summer H200 regression pattern shows weaker height gradients over northern and central China as the springtime anomalous low over Mongolia weakens and retreats to the northwest of its spring position (Figure 11b). The negative sea-level pressure anomaly centre remains north of China, and the positive pressure anomaly

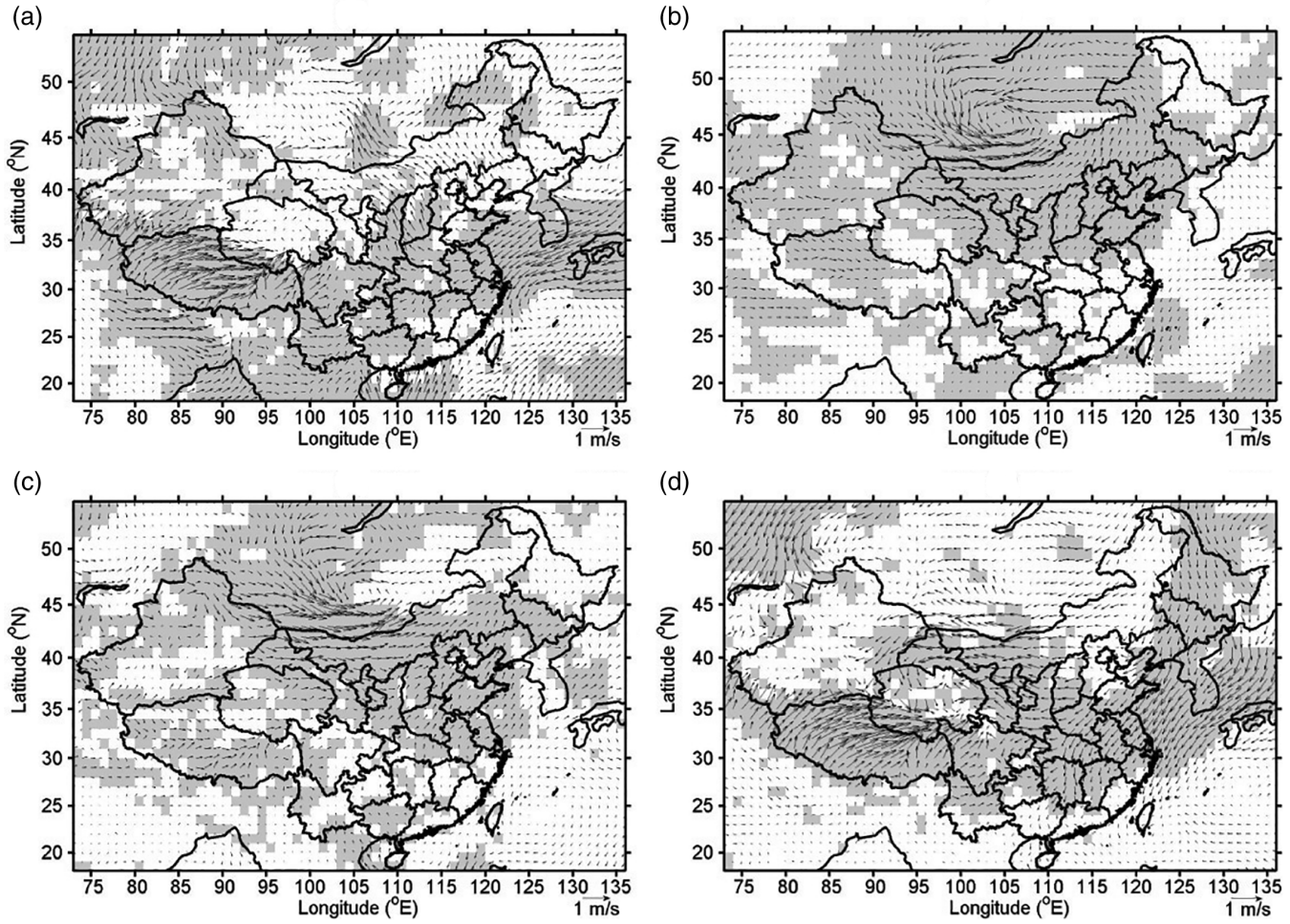

FIGURE 7 The anomalous 80-m wind vectors regressed onto the PC1 of the 80-m wind speed seasonal anomalies for spring (a), summer (b), autumn (c), and winter (d) for the period 1979 to 2011. The shaded regions are significant at the 95% confidence level

centre moves southwestward from Qinghai to Tibet (Figure 12b). The cyclonic flows associated with the anomalous low and the anticyclonic flows associated with the anomalous high (Figure 13b) result in positive wind speed anomalies over northern Inner Mongolia and negative wind speed anomalies over Tibet (Figure 10b). The H200, sea-level pressure, and wind vector regression patterns for autumn (Figures 11c, 12c, and 13c) are similar to those of summer, although the strengths and positions of the lows and highs are slightly different.

In winter, the regression patterns of the H200 anomalies bear a remarkable resemblance to that of the negative phase of the AO, with positive height anomalies over the high latitudes and negative anomalies over the mid- and low-latitudes (Figure 11d). Negative sea-level pressure anomalies are found over most of China, except for Xinjinag, Quinghai and Tibet (Figure 12d). The corresponding anomalous westerly winds (Figure 13d) explain the positive wind speed anomalies over northern China (Figure 10d). Strong westerly winds are also found in Qinghai as the anticyclonic winds around the anomalous high to the south and cyclonic flow around the anomalous low to the north merge over the region, which explains the strong positive wind speed anomalies there (Figure 10d). Easterly winds around the anomalous high in southern Tibet are consistent with the negative wind speed anomalies in that region.

The results above suggest a connection between the EOF2 mode and the AO in spring and particularly in winter. This connection is further confirmed by the strong correlations between the seasonal anomalies of the 80-m wind speeds and the AO index (Figure 14). For both seasons, the spatial patterns of the correlations are almost mirror images of the EOF2 patterns, indicating that the 80-m wind speeds are inversely related to the AO at nearly all locations across the country. During spring, significant negative correlations are found over southeastern China and portions of southwestern China. Significant positive correlations are found in areas of northwestern and northeastern China and southern part of the Tibetan Plateau. During the winter, significant negative correlations exist over northern China, while significant positive correlations occur over much of Tibet and areas of southeastern, northwestern, and northeastern China.

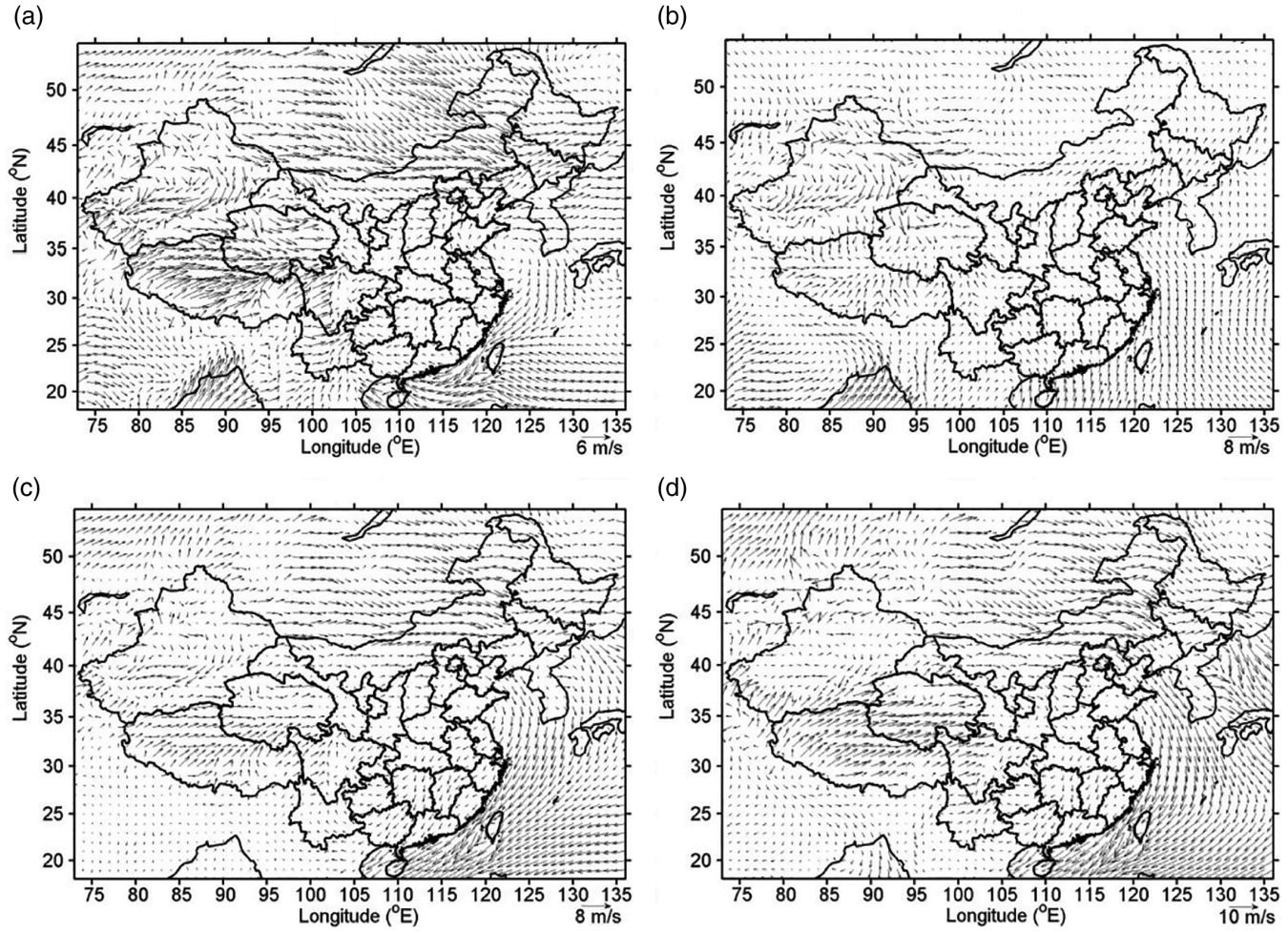

FIGURE 8 Mean wind vector fields over the study domain for spring (a), summer (b), autumn (c), and winter (d) for the period 1979–2011

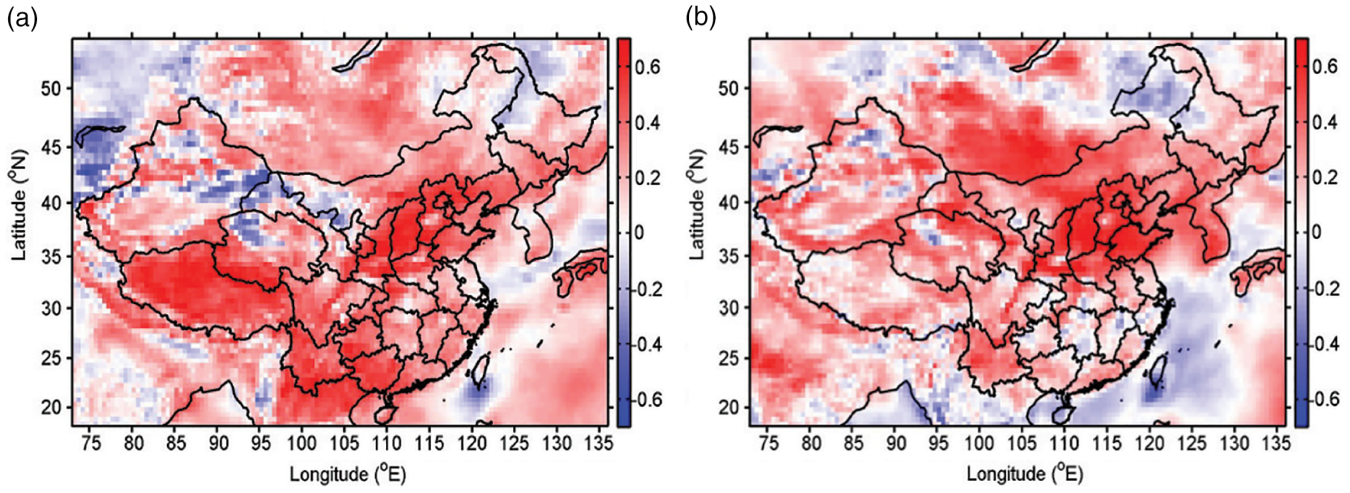

FIGURE 9 Correlations between 80-m wind speed seasonal anomalies and the PDO indices for summer (a) and autumn (b). Correlation coefficients with magnitudes >0.34 are statistically significant at the 95% confidence level [Colour figure can be viewed at wileyonlinelibrary.com]

4 | SUMMARY

In this study, the interannual variability of seasonal wind speeds at the modern wind turbine level (80-m AGL) across China is examined using the CFSRv2 data. The EOF technique is utilized to identify spatial modes of the variability and how those modes change with time over the 1979–2011 period. The first two leading EOF modes are explained in the context of large-scale atmospheric circulations via regression and correlation analyses.

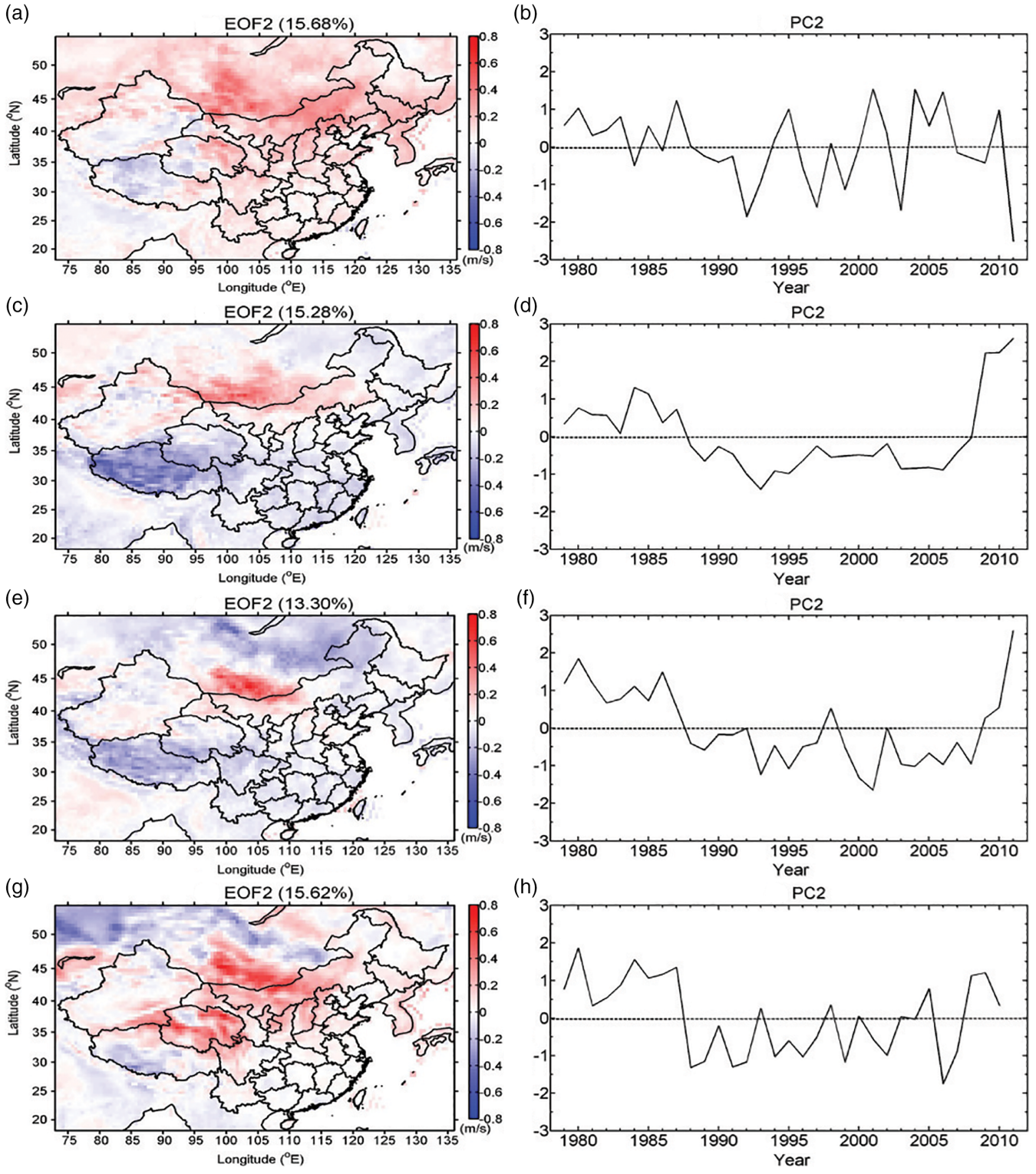

FIGURE 10 EOF2 spatial patterns (a, c, e, g) and time series (b, d, f, h) for the 80-m wind speed seasonal anomalies for spring (a, b), summer (c, d), autumn (e, f) and winter (g, h) for the period 1979 to 2011 [Colour figure can be viewed at wileyonlinelibrary.com]

The first EOF mode accounts for approximately 23% for spring and winter and 29% for summer and autumn of the total variance in the seasonal anomalies of 80-m level wind speeds. The spatial patterns are similar during summer and autumn, showing in-phase variability across much of China with stronger variability in northern portions of the country and over Tibet. The patterns are similar during spring and winter, where the variability is out of phase between northern and southern China (separated roughly by the 35°N latitude line), with largest contrast between Tibet and Inner Mongolia.

The first EOF mode is statistically associated with the SST anomalies over the Pacific Ocean, particularly during

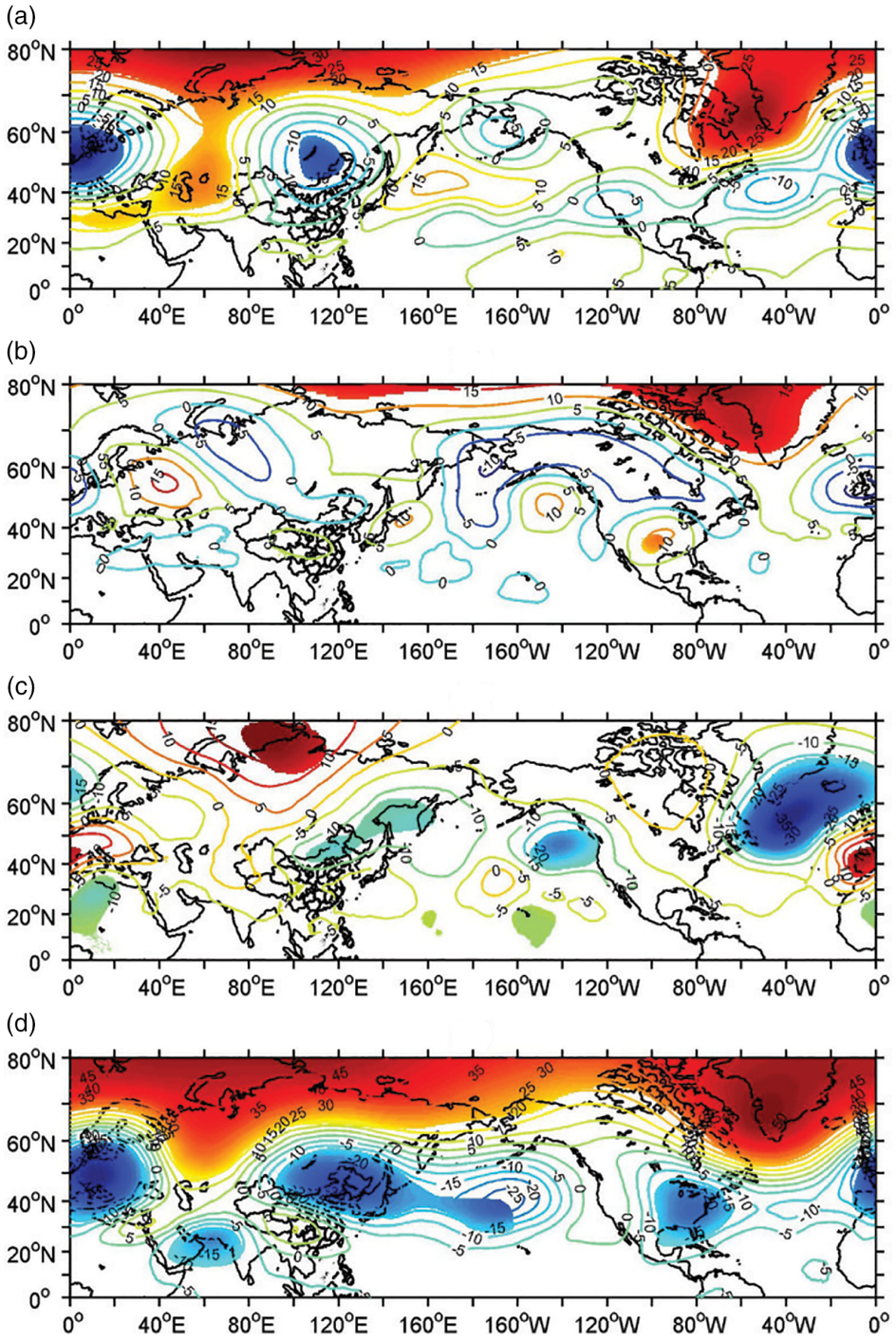

FIGURE 11 The anomalous 200-hPa geopotential heights regressed onto PC2 of the 80-m wind speed seasonal anomalies for spring (a), summer (b), autumn (c), and winter (d) for the period 1979 to 2011. The colour filled regions are significant at the 95% confidence level [Colour figure can be viewed at wileyonlinelibrary.com]

summer and autumn when the PC1 time series are positively correlated with the PDO indices. The decreasing trends in the PDO indices may explain the decreasing trends of the seasonal mean 80-m wind speeds for summer and autumn for the study period of 1979 to 2011. During the positive phase of the PDO index, the 200-hPa height anomalies are predominantly negative over most of China, and a significant negative sea-level pressure anomaly centre appears over Mongolia. The westerly anomalous winds on the south side of this anomalous cyclone lead to positive wind speed anomalies across China, and especially over northern China, by reinforcing the climatological wind pattern. The opposite occurs in summer and autumn during the negative phase of the PDO index. During spring and winter, the Pacific North American (PNA) wavetrain excited by the anomalous SST over the tropical Pacific

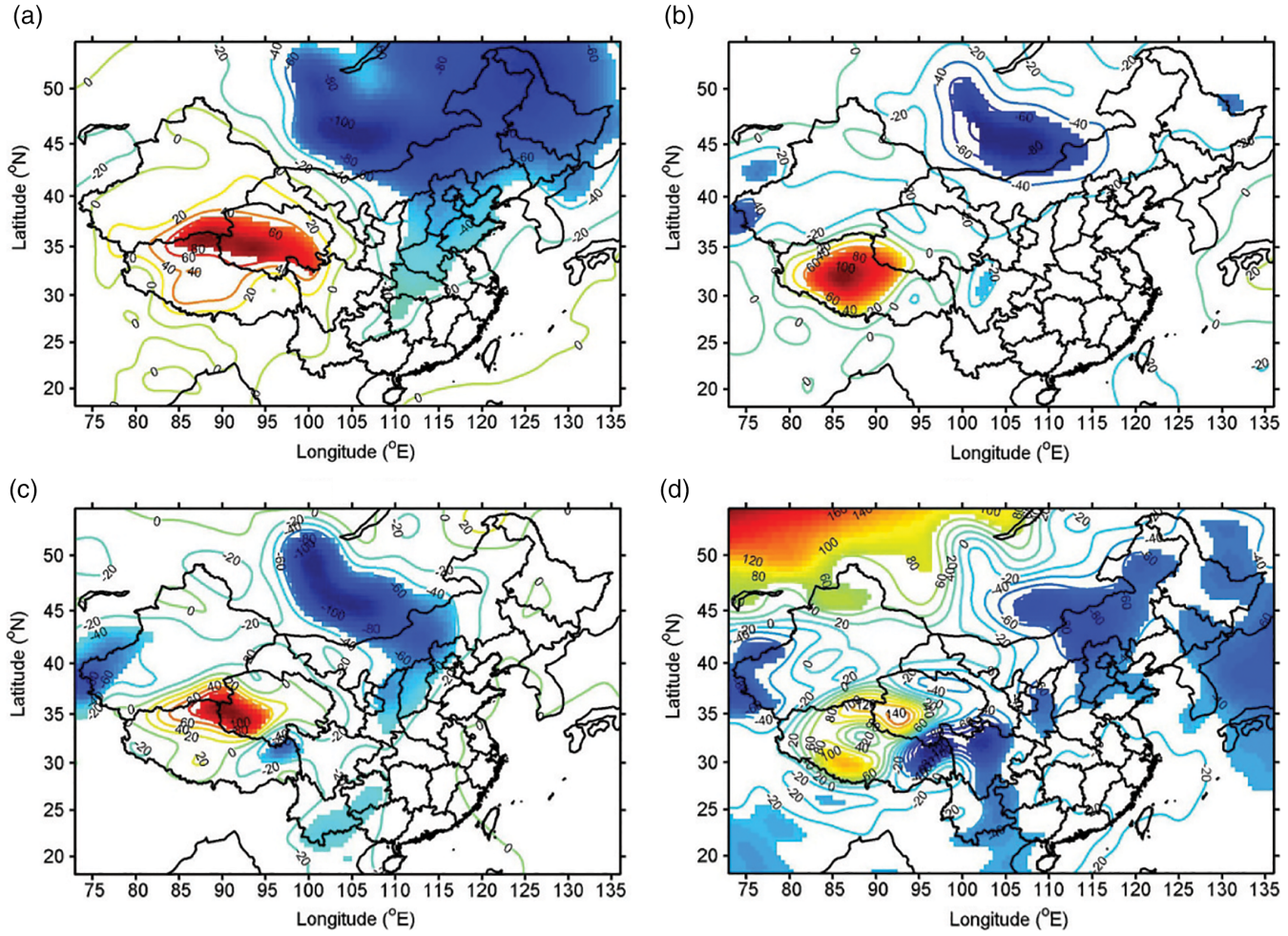

FIGURE 12 The anomalous sea-level pressures regressed to the PC2 of the 80-m wind speed seasonal anomalies for spring (a), summer (b), autumn (c), and winter (d) for the period 1979 to 2011. The filled regions are significant at the 95% confidence level [Colour figure can be viewed at wileyonlinelibrary.com]

Ocean influences the circulations over China. The coupling of a strong anomalous surface low centred over Tibet in winter and over Qinghai in spring with an anomalous high over northeastern China produces southwesterly flows in Tibet and northeasterly flows in northern China and particularly over Inner Mongolia, leading to opposite changes in wind speed in the two regions.

The second EOF mode accounts for 13% (autumn) to 16% (spring and winter) of the total variance in the seasonal anomalies of the 80-m level wind speeds. Like the first EOF mode, the spatial patterns are similar between spring and winter, and between summer and autumn. The spring and winter pattern is characterized by negative wind speed anomalies over the Tibetan Plateau and portions of northwestern China and positive anomalies over the rest of the country, especially in the northern and northeastern regions. The contrast in wind speed anomalies is stronger in winter than spring. For both seasons, the second EOF mode appears to be inversely related to the AO climate mode, with the positive phase of the AO associated with a weakening (strengthening) of winds in most regions (Tibet and portions of northwestern China). The opposite occurs during the negative phase of the AO. The spatial patterns for summer and autumn are characterized by positive wind speed anomalies over Inner Mongolia and northwestern China and negative anomalies over the rest of China, particularly in the Tibetan Plateau region. These patterns can be largely explained statistically by the opposite sea-level pressure changes and the associated anomalous flows between Mongolia and the Tibetan Plateau. The PCs for the second mode (PC2) for summer and autumn exhibit a variability at interdecadal time scales.

The connection between the SST anomalies and wind power variations in China is highlighted by the schematic diagram in Figure 15. It is worth noting that the results here are based solely on statistical analyses. Although they may be useful in revealing possible teleconnections between the interannual variability of wind energy resources across China and changes in large-scale circulations, they do not prove causation. Other limitations of the current analyses include the use of the coarse resolution gridded reanalysis data that are unlikely to resolve local factors such as topography and land use heterogeneity that might affect low-level

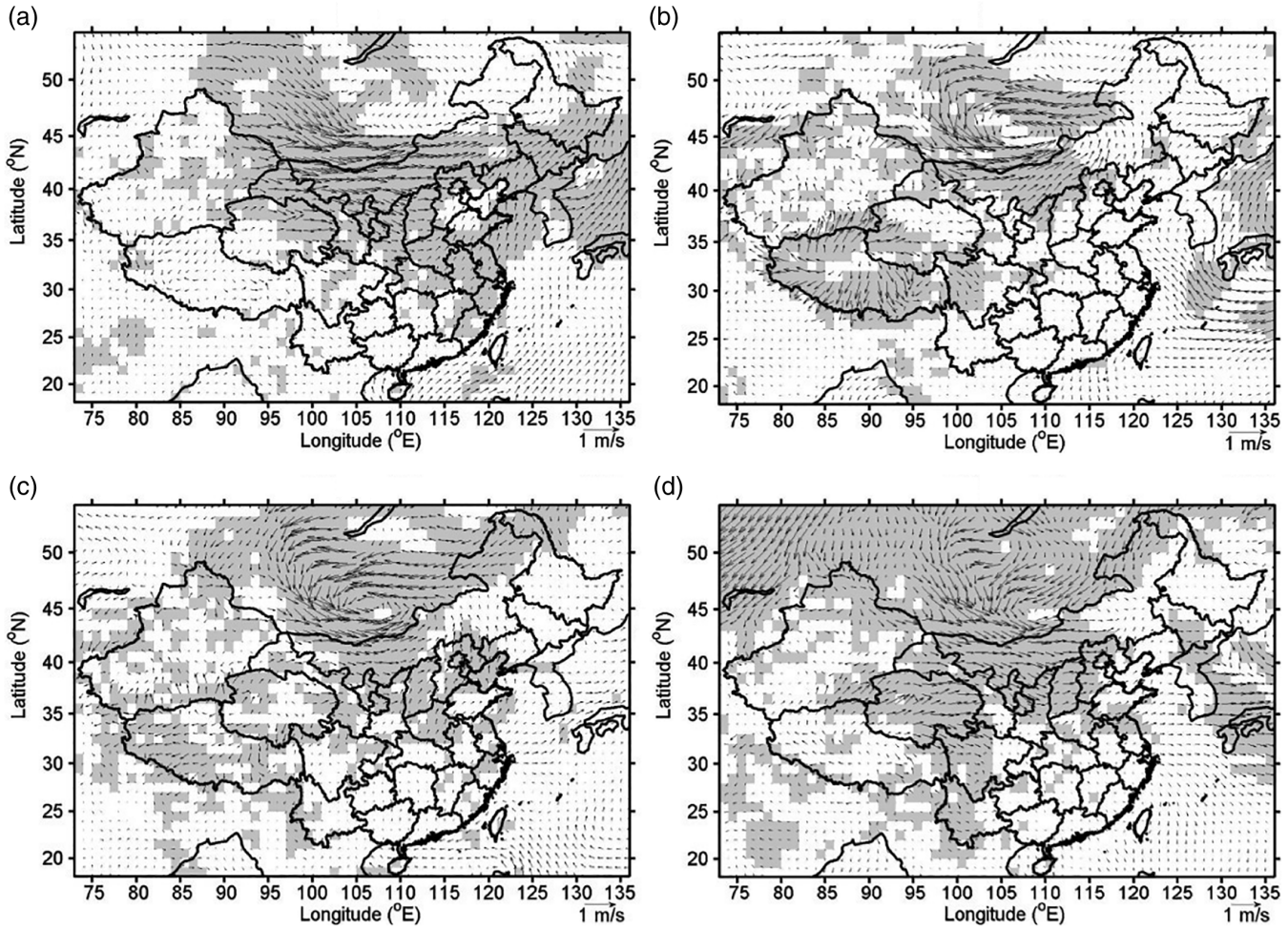

FIGURE 13 The anomalous 80-m wind vectors regressed onto the PC2 of the 80-m wind speed seasonal anomalies for spring (a), summer (b), autumn (c), and winter (d) for the period 1979 to 2011. The shaded regions are significant at the 95% confidence level

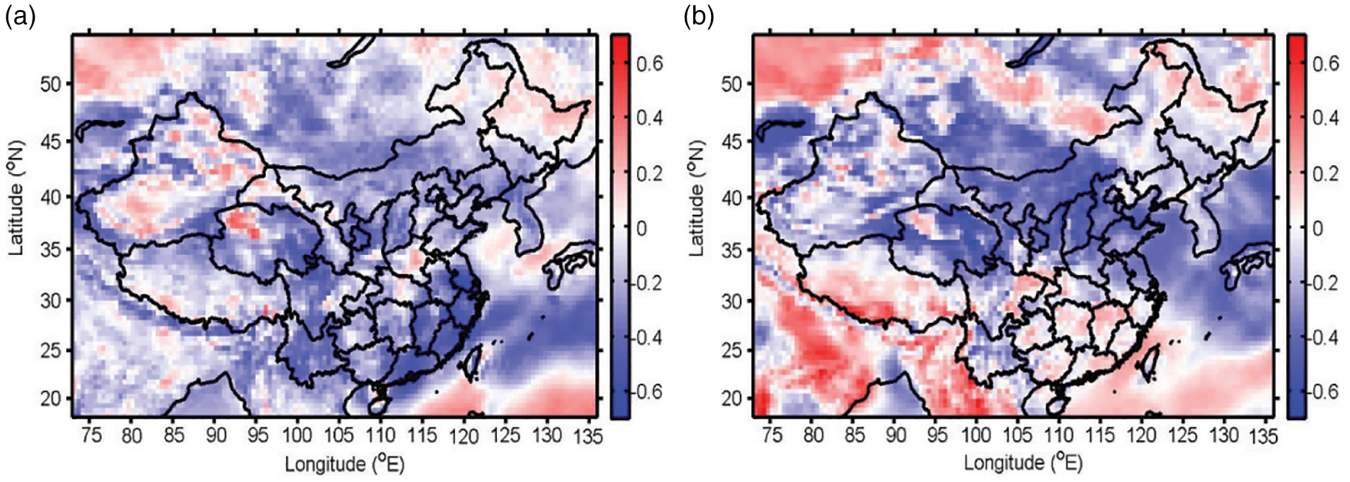

FIGURE 14 Correlations between the 80-m wind speed seasonal anomalies and the AO indices for spring (a) and winter (b). Correlation coefficients with magnitudes greater than 0.34 are statistically significant at the 95% confidence level [Colour figure can be viewed at wileyonlinelibrary.com]

winds. Despite the limitations, the spatiotemporal patterns of wind energy resources across China and their association with large-scale circulation anomalies may prove useful to the wind energy industry in China. Although wind energy resources vary on a time scale of an hour or less, policy makers are concerned about seasonal information of wind energy production for a given season. Hence, understanding seasonal mean wind and its connection to large-scale circulation patterns can help improve seasonal forecasting of wind resources.

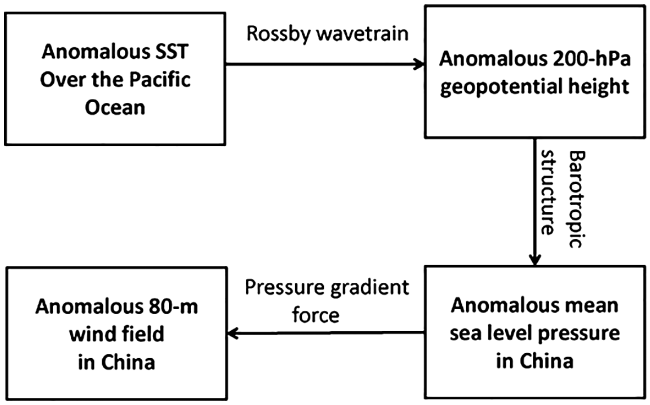

FIGURE 15 A schematic diagram highlighting the connection between the occurrence of anomalous SSTs in the Pacific Ocean to the occurrence of anomalous 80-m wind fields in China

ACKNOWLEDGEMENTS

The authors thank the efforts made by NCEP in producing the CFSR data. This research was supported by the Shanghai Pujiang Program (No. 17PJ1409800).

ORCID

Lejiang Yu https://orcid.org/0000-0003-0535-1937
Shiyuan Zhong https://orcid.org/0000-0002-2287-7220

REFERENCES

Bao, X. and Zhang, F. (2013) Evaluation of NCEP-CFSR, NCEP-NCAR, ERA-Interim, and ERA-40 reanalysis datasets against independent sounding observations over the Tibetan Plateau. *Journal of Climate*, 26, 206–214.

Chan, J.C.L. and Zhou, W. (2005) PDO, ENSO and the early summer monsoon rainfall over South China. *Geophysical Research Letters*, 32, L08810. https://doi.org/10.1029/2004GL022015.

Chen, L., Li, D. and Pryor, S.C. (2013) Wind speed trends over China: quantifying the magnitude and assessing causality. *International Journal of Climatology*, 33, 2579–2590.

Chen, G., Iwasaki, T., Qin, H. and Sha, W. (2014) Evaluation of the warm-season diurnal variability over East Asia in recent reanalyses JRA-55, ERA-Interim, NCEP CFSR, and NASA MERRA. *Journal of Climate*, 27, 5517–5537.

Cui, X., Dong, Z., Sun, H., Li, C., Xiao, F., Liu, Z., Song, S., Li, X., Xiao, N. and Xiao, W. (2018) Spatial and temporal variation of the near-surface wind environment in the dune fields of northern China. *International Journal of Climatology*, 38, 2333–2351.

Dee, D.P., Uppala, S.M., Simmons, A.J., Berrisford, P., Poli, P., Kobayashi, S., Andrae, U., Balmaseda, M.A., Balsamo, G., Bauer, P., Bechtold, P., Beljaars, A.C.M., van de Berg, L., Bidlot, J., Bormann, N., Delsol, C., Drgani, R., Fuentes, M., Geer, A.J., Haimberger, L., Healy, S.B., Hersbach, H., Hólm, E.V., Isaksen, L., Kållberg, P., Köhler, M., Matricardi, M., McNally, A.P., Monge-Sanz, B.M., Morcrette, J.J., Park, B.-K., Peubey, C., de Rosnay, P., Tavolato, C., Thépaut, J.-N. and Vitart, F. (2011) The ERA-Interim reanalysis: configuration and performance of the data assimilation system. *Quarterly Journal of the Royal Meteorological Society*, 137, 553–597. https://doi.org/10.1002/qj.828.

Draper, N.R. and Smith, H. (1998) *Applied Regression Analysis*, 3rd edition. Wiley-Interscience: New York, NY, 736pp.

Ebita, A., Kobayashi, S., Ota, Y., Moriya, M., Kumabe, R., Onogi, K., Harada, Y., Yasui, S., Miyaoka, K., Takahashi, K., Kamahori, H., Kobayashi, C., Endo, H., Soma, M., Oikawa, Y. and Ishimizu, T. (2011) The Japanese 55-year reanalysis "JRA-55": an interim report. *SOLA*, 7, 149–152. https://doi.org/10.2151/sola.2011-038.

Fu, G., Yu, J., Zhang, Y. and Hu, S. (2011) Temporal variation of wind speed in China for 1961-2007. *Theoretical and Applied Climatology*, 104, 313–324.

Gong, D.-Y. and Ho, C.-H. (2003) Arctic oscillation signals in the East Asian summer monsoon. *Journal of Geophysical Research*, 108, 4006. https://doi.org/10.1029/2002JD002193.

Gong, D.-Y., Wang, S.-W. and Zhu, J.-H. (2001) East Asian winter monsoon and arctic oscillation. *Geophysical Research Letters*, 28, 2073–2076.

Hsu, S.A., Meindl, E.A. and Gilhousen, D.B. (1994) Determining the power-law wind-profile exponent under near-neutral stability conditions at sea. *Journal of Applied Meteorology*, 33, 757–765.

Jiang, L., Chi, Y., Qin, H., Pei, Z., Li, Q., Liu, M., Bai, J., Wang, W., Feng, S., Kong, W. and Wang, Q. (2011) Wind energy in China. *IEEE Power & Energy Magazine*, 9, 36–46.

Jiang, Y., Luo, Y. and Zhao, Z. (2013) Maximum wind speed changes over China. *Acta Meteorologica Sinica*, 27, 63–74.

Li, J., Cai, F., Qiao, L., Xie, H., Hu, G., Yang, X., Tang, W., Wang, W., Li, X. (2012). *China wind energy outlook 2012*. Global Wind Energy Council. Available at: http://www.gwec.net/publications/country-reports/china-wind-energy-outlook-2012/ [accessed 9th August 2018].

Lin, C., Yang, K., Qin, J. and Fu, R. (2013) Observed coherent trends of surface and upper-air wind speed over China since 1960. *Journal of Climate*, 26, 2891–2903.

Mantua, N.J., Hare, S.R., Zhang, Y., Wallace, J.M. and Francis, R.C. (1997) A Pacific interdecadal climate oscillation with impacts on salmon production. *Bulletin of the American Meteorological Society*, 78, 1069–1079.

McElroy, M.B., Lu, X., Nielsen, C.P. and Wang, Y. (2009) Potential for wind-generated electricity in China. *Science*, 325, 1378–1380.

Neter, J., Wasserman, W. and Kutner, M.H. (1996) *Applied Linear Statistical Models*. McGraw-Hill Irwin: New York, NY, 1408pp.

Niu, F., Li, Z., Li, C., Lee, K.-H. and Wang, M. (2010) Increase of wintertime fog in China: potential impacts of weakening of the Eastern Asian monsoon circulation and increasing aerosol loading. *Journal of Geophysical Research*, 115, D00K20. https://doi.org/10.1029/2009JD013484.

Rahim, N.A.A., Juneng, L. and Tangang, F.T. (2013) Wind-wave simulation in South China Sea: preliminary results of model evaluation using different wind forcing. In: *Proceedings of the Universiti Kebangsaan Malaysis*. American Institute of Physics: Selangor, Malaysia, 454–459. https://doi.org/10.1063/1.4858697.

Rienecker, M.R., Suarez, M.J., Gelaro, R., Todling, R., Bacmeister, J., Liu, E., Bosilovich, M.G., Schubert, S.D., Takacs, L., Kim, G.-K., Bloom, S., Chen, J., Collins, D., Conaty, A., da Silva, A., Gu, W., Joiner, J., Koster, R. D., Lucchesi, R., Molod, A., Owens, T., Pawson, S., Pegion, P., Redder, C. R., Reichle, R., Robertson, F.R., Ruddick, A.G., Sienkiewicz, M. and Woollen, J. (2011) MERRA: NASA's modern-era retrospective analysis for research and applications. *Journal of Climate*, 24, 3624–3648. https://doi.org/10.1175/JCLI-D-11-00015.1.

Saha, S., Moorthi, S., Pan, H.-L., Wu, X., Wang, J., Nadiga, S., Tripp, P., Kistler, R., Woollen, J., Behringer, D., Liu, H., Stokes, D., Grumbine, R., Cayno, G., Wang, J., Hou, Y.-T., Chuang, H.-Y., Juang, H.-M.H., Sela, J., Iredell, M., Treadon, R., Kleist, D., Delst, P.V., Keyser, D., Derber, J., Ek, M., Meng, J., Wei, H., Yang, R., Lord, S., Dool, H.V.D., Kumar, A., Wang, W., Long, C., Chelliah, M., Xue, Y., Huang, B., Schemm, J.-K., Ebisuzaki, W., Liu, R., Xie, P., Chen, M., Zhou, S., Higgins, W., Zou, C.-Z., Liu, Q., Chen, Y., Han, Y., Cucurull, L., Reynolds, R.W., Rutledge, G. and Goldberg, M. (2010) The NCEP climate forecast system reanalysis. *Bulletin of the American Meteorological Society*, 91, 1015–1057.

Saha, S., Moorthi, S., Wu, X., Wang, J., Nadiga, S., Tripp, P., Behringer, D., Hou, Y.-T., Chuang, H., Iredell, M., Ek, M., Meng, J., Yang, R., Mendez, M.P., van den Dool, H., Zhang, Q., Wang, W., Chen, M. and Becker, E. (2014) The NCEP climate forecast system version 2. *Journal of Climate*, 27, 2185–2208.

Stull, R.B. (1988) *An Introduction to Boundary Layer Meteorology*. London: Kluwer Academic Publishers 666 pp.

Wang, B. and Lin, H. (2002) Rainy seasons of the Asian-Pacific monsoon. *Journal of Climate*, 15, 386–398.

Wang, B., Wu, R. and Fu, X. (2000) Pacific-East Asian teleconnection: how does ENSO affect East Asian climate? *Journal of Climate*, 13, 1517–1536.

Watanabe, M. (2004) Asian jet waveguide and a downstream extension of the North Atlantic Oscillation. *Journal of Climate*, 17, 4674–4691.

Westrick, K.J., Storck, P. and Hiester, T. (2005) Improving the economics of wind through forecasting. *North American Windpower*, 2, 20–22.

Wilks, D.S. (2011) *Statistical Methods in the Atmospheric Sciences*. Elsevier Academic Press: San Diego, CA, 676 pp.

Wu, Z., Wang, B., Li, J. and Jin, F.-F. (2009) An empirical seasonal prediction model of the east Asian summer monsoon using ENSO and NAO. *Journal of Geophysical Research*, 114, D18120.

Wu, J., Zha, J. and Zhao, D. (2016) Estimating the impacts of the changes in land use and cover on the surface wind speed over the East China Plain during the period 1980-2011. *Climate Dynamics*, 46, 847–863.

Wu, J., Zha, J.L. and Zhao, D.M. (2017) Evaluating the effects of land use and cover change on the decrease of surface wind speed over China in recent 30 years using a statistical downscaling method. *Climate Dynamics*, 48, 131–149.

Xu, M., Chang, C.-P., Fu, C., Qi, Y., Robock, A., Robinson, D. and Zhang, H. (2006) Steady decline of East Asian monsoon winds, 1969-2000: evidence from direct ground measurements of wind speed. *Journal of Geophysical Research*, 111, D24111. https://doi.org/10.1029/2006JD007337.

Yao, H. and Li, D. (2016) The interannual variation of wind speed in the Tibetan Plateau in spring and its response to global warming during 1971-2012. *Acta Meteorologica Sinica*, 74, 60–75.

Yoon, J. and Yeh, S.W. (2010) Influence of the Pacific decadal oscillation on the relationship between El Niño and the northeast Asian summer monsoon. *Journal of Climate*, 23, 4525–4537.

Yu, L., Zhong, S., Bian, X. and Heilman, W.E. (2016) Climatology and trend of wind power resources in China and its surrounding regions: a revisit using climate forecast system reanalysis data. *International Journal of Climatology*, 36, 2173–2188. https://doi.org/10.1002/joc.4485.

Zha, J.L., Wu, J. and Zhao, D.M. (2017) Effects of land use and cover changes on the near-surface wind speed over China in the last 30 years. *Progress in Physical Geography*, 23, 46–67. https://doi.org/10.1177/0309133316663097.

Zhang, Z., Yang, Y., Zhang, X. and Chen, Z. (2014) Wind speed changes and its influencing factors in Southwestern China. *Acta Ecologica Sinica*, 34, 471–481.

Zuo, H., Li, D., Hu, Y., Bao, Y. and Lu, S. (2005) Characteristics of climatic trends and correlation between pan-evaporation and environmental factors in the last 40 years over China. *Chinese Science Bulletin*, 50, 1235–1241.

How to cite this article: Yu L, Zhong S, Bian X, Heilman WE. The interannual variability of wind energy resources across China and its relationship to large-scale circulation changes. *Int J Climatol*. 2019; 39:1684–1699. https://doi.org/10.1002/joc.5909